Electron Beam Fabrication of Birefringent Microcylinders

Zhuangxiong Huang,† Francesco Pedaci,† Maarten van Oene, Matthew J. Wiggin, and Nynke H. Dekker*

Department of Bionanoscience, Kavli Institute of Nanoscience, Faculty of Applied Sciences, Delft University of Technology, Lorentzweg 1 2628 CJ, Delft, The Netherlands. † These authors contributed equally to this work.

ABSTRACT Numerous biological and biotechnological applications rely on the use of micrometer- and nanometer-scale particles, benefiting tremendously from quantitative control of their physical and chemical properties. Here, we describe the use of electron beam lithography for the design, fabrication, and functionalization of micrometer-scale birefringent quartz cylinders for use in sensing and detection. We demonstrate excellent control of the cylinders' geometry, fabricating cylinders with heights of 0.5−2 μm and diameters of 200−500 nm with high precision while maintaining control of their side-wall angle. The flexible fabrication allows cylinders to be selectively shaped into conical structures or to include centered protrusions for the selective attachment of biomolecules. The latter is facilitated by straightforward functionalization targeted either to a cylinder's face or to the centered protrusion alone. The fabricated quartz cylinders are characterized in an optical torque wrench, permitting correlation of their geometrical properties to measured torques. Lastly, we tether individual DNA molecules to the functionalized cylinders and demonstrate the translational and rotational control required for single-molecule studies.

KEYWORDS: birefringent particles · quartz microcylinders · electron-beam lithography · nanofabrication · surface functionalization · optical tweezers · optical torque wrench

A variety of micrometer-sized particles find application in biological separation,[1] biophysical techniques such as magnetic and optical tweezers,[2−4] the preparation of colloidal suspensions and the study of their physical properties,[5,6] or the construction of artificial devices such as nanoscale swimmers.[7] Both the physical and chemical properties of such particles, for example, their ferromagnetic or paramagnetic character, value of their dielectric constant, and surface coating, play a role in their applicability. Birefringent particles, based on materials capable of exchanging spin angular momentum with light (Figure 1a), are also of great interest. They have been exploited in microrheology as sensors to measure properties of the surrounding fluid,[8−10] in microfluidics as micrometer-scale pumps for flow generation,[11] and in the torque spectroscopy of single biomolecules[12,13] through their key role in the optical torque wrench.

Several methods exist for the production of birefringent particles, resulting in a variety of forms such as vaterite microspheres,[14,15] tetragonal lysozyme crystals,[16,17] organic semiconductor platelets,[18] $LiNbO_3$ microcrystals,[19] organic dye microcrystals,[20]

For applications in single-molecule torque spectroscopy, which form the primary motivation for our work, quartz constitutes a particularly suitable material,[13,21,22] a consequence of its chemical stability and biological inertness, the facility with which it can be coated, and the control of its geometry.

La Porta *et al.*[22] pioneered the use of birefringent particles in an optical torque wrench (OTW), schematically illustrated in Figure 1. When a birefringent particle is trapped in a focused laser beam, the polarization of the trapping beam can be used to apply a torque to the particle, allowing it to be aligned or continuously spun[23] (Figure 1b). Moreover, in such a configuration the torque exerted on a birefringent particle can be measured directly from the change in angular momentum of the light beam (Figure 1c).[13,21,22] In a particularly elegant implementation of an OTW, the birefringent particles are formed from quartz cylinders; such cylinders will align their long axis with the direction of laser propagation,[16,24] thereby confining two rotational degrees of freedom. Provided that the quartz extraordinary axis is perpendicular to the cylinder's long axis, the third rotational degree of freedom can be controlled by the polarization of the trapping beam. Controlled rotation of the trapping beam polarization results in rotation of the cylinder and, if the cylinder is tethered to a well-anchored DNA, to the build-up of twist in DNA[12] (Figure 1a,b).

Typically, optical lithography has been employed in the fabrication and functionalization of such cylinders, as reported by Deutel *et al.*[21] and Gutierrez-Medina *et al.*[13] However, the use of optical lithography

*Address correspondence to N.H.Dekker@tudelft.nl.

Received for review November 23, 2010 and accepted January 18, 2011.

Published online 10.1021/nn1034108

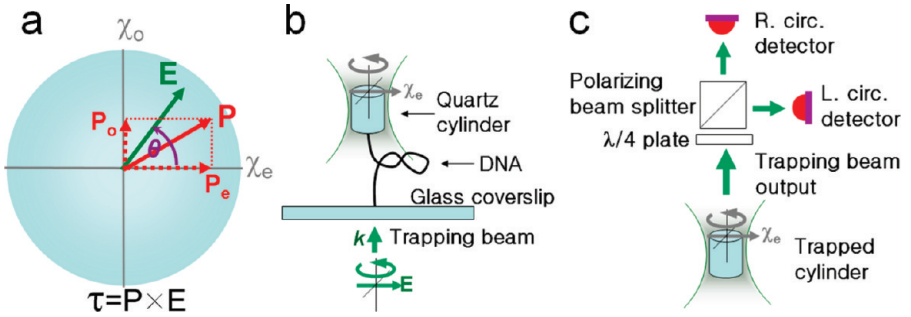

Figure 1. Schematic of an optical torque wrench. (a) The electric susceptibilities differ along the extraordinary axis (χ_e) and the ordinary axis (χ_o) of a birefringent material. Hence, unless the electric field is aligned with either axis, the induced dipole *P* (red vector) is not colinear with external electric field *E* (green vector), resulting in the generation of torque τ. (b) Use of an optical torque wrench for the study of DNA. A birefringent quartz cylinder having its extraordinary axis perpendicular to its cylindrical axis is maintained in an optical trap as shown. Here *k* indicates the propagation direction of the trapping laser beam. The top surface of the cylinder is chemically functionalized to permit the binding of DNA *via* multiple bonds. The DNA's other extremity is attached to a glass coverslip in a flow cell, likewise *via* multiple bonds. By controlled rotation of the trapping beam's linear polarization, the cylinder can be rotated, generating twist in the DNA. (c) Meanwhile, the torque exerted by the trapping laser on the cylinder is measured by a torque detector that records the imbalance in the intensities of the right and left circular components of the transmitted beam.

for making quartz cylinders comes with a number of limitations. Importantly, it restricts the smallest feature sizes to *ca.* 300−400 nm.[13] Here, we report a novel, electron beam lithography-based approach to the nanofabrication and functionalization of quartz cylinders that presents a number of advantages. First, electron beam lithography is capable of patterning a wide range of feature sizes. These can be as small as a few nanometers, making it possible to fabricate smaller cylinders with great ease. Simultaneously, our electron beam-based approach remains very well-suited for the fabrication of larger quartz cylinders, especially those with high aspect ratios. Second, our approach comes with great versatility: cylinders may be modified into having a slightly conical shape or fabricated to include a nanometer-scale centered protrusion for the controlled binding of DNA (thereby reducing overall precession). Third, our approach introduces selective surface functionalization following, rather than prior to, the removal of the etching mask, implying that the choice of etching mask is independent of the chemistry of functional groups and affording a wider choice of etching geometries and cylinder shapes. Using this approach, we demonstrate the fabrication of quartz cylinders with lateral dimensions in the range of 0.5−2 μm and axial dimensions in the range of 200−500 nm. The cylinders can be made to high uniformity (4.2% relative standard deviation (RSD) in volume, and a control of their side angles within an error of 0.3°). We further fabricate cylinders including centered protrusions on one of their two faces, and demonstrate excellent control of cylinder functionalization, functionalizing either a single face of a cylinder or only the centered protrusion itself. We present extensive characterization of the cylinders *via* scanning electron microscopy, biochemical analysis, and optical microscopy. The characterization is completed by introducing the cylinders into an OTW, where we correlate their physical properties to the measured torque signals. We then demonstrate, using well-controlled tethering of DNA to the functionalized cylinders, successful force and torque spectroscopy on an individual biomolecule.

RESULTS AND DISCUSSION

Control of the Physical Properties of Quartz Cylinders. Ideally, quartz cylinders for application in OTW should have the following properties. First, the cylinder's aspect ratio (height:diameter) should be sufficiently large[16] to allow for tight confinement of the long axis of the cylinder along the propagation direction of trapping beam. Second, depending on the specific application, the cylinder size should be tunable: for example, if stronger trapping and larger torques are desired, larger cylinders are appropriate; conversely, smaller cylinders have the advantage of lower noise in the measured torque signal and a smaller drag (resulting in a faster response time). Third, it should be straightforward to attach DNA (or other biomolecules), and preferably so to the center of the cylinder's top or bottom surface.[13] Otherwise, when the DNA is stretched, the cylinder will precess and dramatically increase the noise in the torque measurement.

Fine control of the dimensions and the resulting geometry of the quartz cylinders necessitates a thorough understanding of the physical processes involved in patterning and etching. Using the protocols described in the Methods and illustrated in Figure 2, we were able to fulfill these criteria and fabricate uniform arrays of quartz microcylinders (Figure 3 panels a and e show images of such arrays) in a wide variety of sizes and geometries. For instance, it was possible to control cylinder height (a range of 0.5−2 μm was fabricated; Figure 3a−d), cylinder diameter (a range of 200−500 nm was fabricated; Figure 3a−d), the angle of the cylinder side wall (Figure 3b−d), and whether or

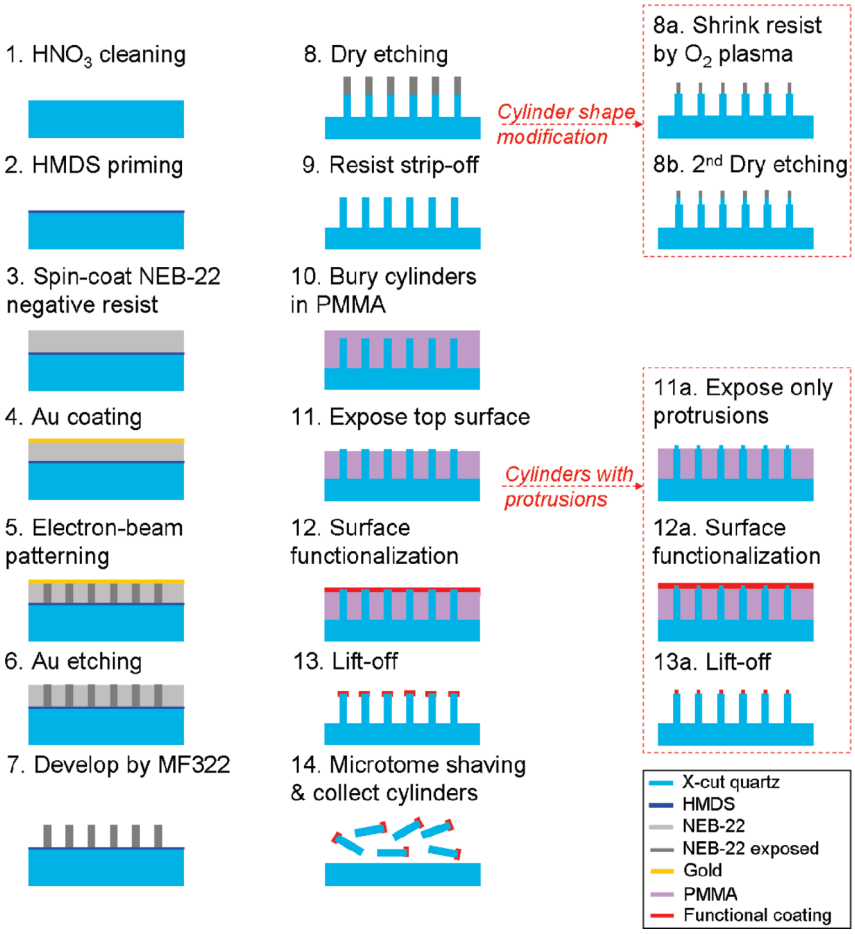

Figure 2. Schematic of the fabrication and selective functionalization of micrometer-scale quartz cylinders using negative-tone electron beam lithography. (Step 1) A single-crystal quartz wafer is cleaned and prepared for patterning. (Steps 2−4) A negative electron beam resist is coated onto the wafer and prepared for electron beam patterning. (Steps 5−7) Electron beam exposure and development of resist posts. (Steps 8 and 9) Dry etching and formation of the quartz cylinders. (Steps 10−13) Selective functionalization of the top surface of the quartz cylinders. (Step 14) Shaving off and collecting of the quartz cylinders. (Steps 8a,b) The formation of centered protrusions. (Steps 11a−13a) Selective functionalization of the quartz cylinders with centered protrusions. For further details, see Methods.

not the cylinder included any protrusions from its center for controlled binding of DNA (Figure 3e−g). We now discuss the control of these parameters.

To control of the diameter of cylinder's top surface, it suffices to control the electron beam patterning. We typically found the difference between the cylinder's diameter (as measured by SEM) and the nominal diameter of the defocused spot of the electron beam to be less than 6% for all wafers of cylinders (Figure 3b−d,f,g). The shape of the cylinder's cross section, which is likewise defined by the electron beam's patterning spot, was similarly easily controlled and exhibited a uniformly round shape over all cylinder sizes tested on various wafers (Figure 3b,c,g).

To control the height (and hence the aspect ratio) of the quartz cylinders, we relied on control of the total etching time, which was demonstrated to be a reliable parameter: for instance, provided that the same machine settings were employed, the etching rate of the C_4F_8 plasma was found to be quite reproducible on different wafers. Additionally, we also found that for cylinders with heights ranging between 0.5 and 2 μm, the etching rate remained approximately stable throughout the time course, that is, any RIE lag could be ignored.[26] However, the etching rate did vary across the wafer, increasing monotonically with the radial distance from the wafer center (5 $\pm$ 2% per 10 mm, as measured by SEM analysis over all wafers). This behavior (known as macro-loading effect[27]) results from the depletion of reactant along its transportation course from outside edge to the wafer center and may be alleviated by increasing the supply of reactants and/or decreasing the etch rate. In practice, to acquire cylinders of sufficiently uniform height, we simply employed a subsection of the wafer area (*e.g.*, a circular area at the wafer center, or, preferably, a circular annulus, which has a smaller radial range for the same patterning area). An alternative approach would be to divide the wafer into compartments and to collect the cylinders separately from each.

In addition to the cylinders' height and diameter, we control their side-wall angle. This parameter can be

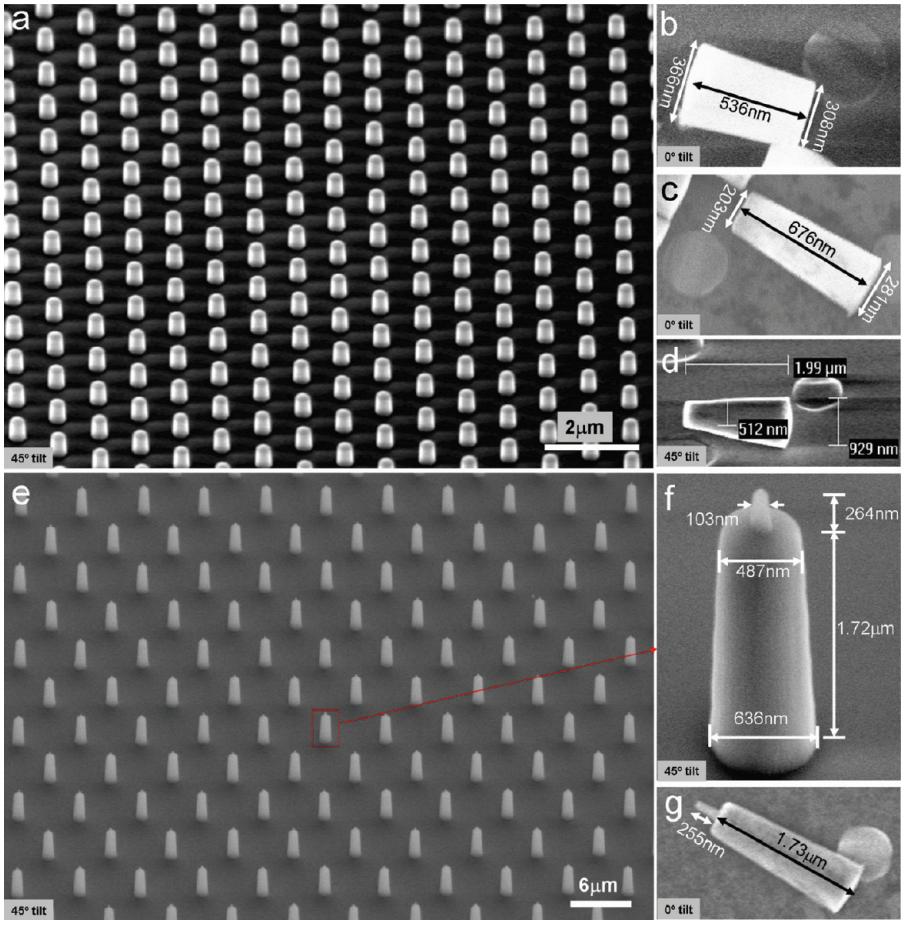

Figure 3. SEM images of fabricated quartz particles. (a) Fabricated quartz cylinders (nominal top diameter: 300-nm) arranged in a hexagonal array pattern on the wafer. (b) A single quartz cylinder after microtome shaving off the wafer (from the same wafer as in panel a). The microtome shaving consistently produces an evenly cut surface at the base of the quartz cylinder, and the cross section of the cut surface demonstrates a round shape at the cylinder's base. (c) A cylinder with a smaller diameter (nominal top diameter: 200 nm) and a higher aspect ratio. (d) A larger cylinder (nominal top diameter: 500 nm) fabricated with a slightly more conical shape. (e−g) Larger cylinders (nominal top diameter: 500 nm) with centered protrusions. (e) Demonstration that the centered protrusions were fabricated consistently on all cylinders in the patterned area. (f) A typical feature size of the centered-protrusion cylinder. (g) A single cylinder with a centered protrusion following microtome shaving. In all panels, the tilt angle of the wafer surface for SEM imaging is indicated in the bottom-left corner.

tuned with ease by tuning the substrate bias power during C_4F_8 plasma dry etching. For example, for a resist mask with features of 500 nm diameter, 1.4 μm height, and 3 μm hexagonal pitch, reducing the bias power from 300 to 250 W decreased the cylinder side wall angle from ~88° to ~84° while leaving the etch rate unchanged (Figure 3d). This dependence of the side wall angle on the substrate bias power may derive from competition between ion bombardment and simultaneous fluorine−carbon polymer deposition: under reduced substrate bias power the sidewall would experience weaker bombardment, permitting a more rapid accumulation of polymer on the side-wall and a concomitant reduction in sidewall angle.[26,28] We note further that the observed insensitivity of the etching rate to the bias power suggests that the etching process is predominantly governed by chemical reactions on the surface,[27] in agreement with the above observation of the macroloading effect.

We note that the above-mentioned guidelines do not take into account the design of the resist mask pattern. However, as the dry etching rate depends on the local geometry, this is also a parameter of interest. Optimization of C_4F_8 plasma conditions was essential in order to guarantee the reproducibility of the dry etching recipe; however, instead of reoptimizing the etching conditions for different resist mask patterns, we found that we could also adapt the local geometry to maintain approximately uniform C_4F_8 plasma settings. Initially, the machine settings for C_4F_8 plasma dry etching (Methods) were optimized for a resist mask with a thickness of 380 nm, encoding for 300 nm diameter features in a 1 μm-pitch hexagonal array (yielding cylinders as in Figure 3a,b). Identical etching settings could be applied to resist masks that had a smaller feature diameter (e.g., 200 nm, Figure 3c), resulting in the same etching rates and sidewall angles. However, when the resist mask had a larger thickness (1.4 μm) and encoded a larger feature diameter (500 nm), we observed an undesirable deposition

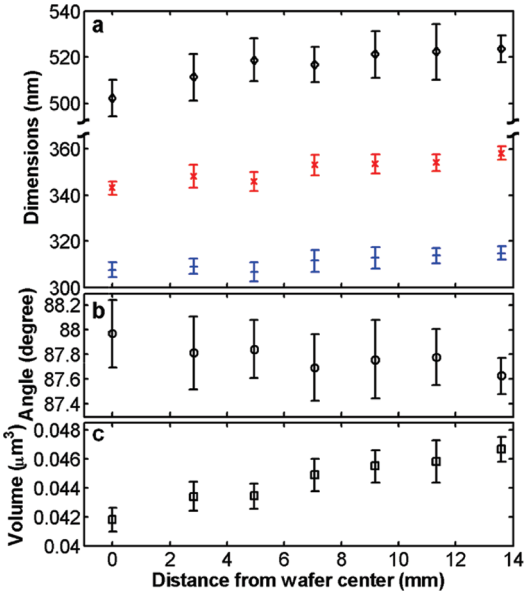

Figure 4. Dimensions of fabricated cylinders on a quartz wafer as a function of radial distance from the wafer center. The nominal top diameter equals 300 nm. (a) Average cylinder heights (black), diameters of cylinder tops (blue), and diameters of cylinder bottoms (red), determined from SEM images. (b) Average cylinder sidewall angles and (c) average cylinders volumes were calculated using the data in panel a. The error bars in all panels represent one standard deviation from the mean.

of Teflon-like polymer onto the quartz, as opposed to quartz etching.

By examining the role of pattern geometry, we can both understand and reduce unwanted polymeric deposition. First, larger and thicker mask features have an increased resist surface area exposed to etching plasma. For a given array pitch, an increase in the exposed resist surface results in an increased amount of resist erosion and a concomitant reduction of the local fluorine-to-carbon ratio. This would tend to favor the deposition of fluorine−carbon polymers over quartz etching. Second, such geometric conditions result in a higher aspect ratio of the etched area between resist mask features, for which a lower etching rate typically ensues.[29,30] This is mainly attributed to a decrease in the transport rate of incoming etching species to the bottom of the etched feature.[29,30] If the increase in mask feature size causes the etch rate to fall below the rate of polymer deposition, the latter will be favored. To successfully circumvent this difficulty, we increased the array pitch of the resist mask to achieve more-or-less equivalent geometries, yielding a resist mask pattern with 500 nm feature diameter, 1.4 μm thickness, and 3 μm pitch (in which both the ratio of the exposed resist surface to the etched quartz surface and the aspect ratio of the etched feature were largely maintained with respect to the original pattern described above). With this adaptation, identical machine settings could be applied, resulting in nearly the same etching rate and side-wall angle (87.8° ± 0.4°, see Figure 3b,c,g for differently sized cylinders).

To examine the variability in cylinder geometries across a wafer, we have performed quantitative SEM measurements (Methods). Here, cylinders were fabricated using a 300 nm defocused electron spot that patterned a resist mask with a thickness of 380 nm; the hexagonal array pitch equaled 1 μm; a circular area of about 14 mm in radius was employed, yielding ~0.7 billion cylinders; and the dry etching time was 3 min. Overall, the cylinders are highly uniform as shown in Figure 4: the cylinder height increases by 4.3% (±2.0%) from wafer center to the outmost pattern position (14 mm from wafer center); the relative standard deviation (RSD) in top diameter is estimated to be 1.5% and 1.7% in bottom diameter; and the computed cylinder side-wall angle is nearly constant: 87.8° ± 0.3°. Overall, the RSD in the volume of quartz cylinder is estimated to be ~4.2% for whole cylinder population. Note that for applications of quartz cylinders in an OTW, the variation in the volume is the most appropriate indicator of cylinder dispersity, as both the optical torque exerted on the cylinder and the rotational drag are approximately proportional to the cylinder volume.

Selective Functionalization of Fabricated Quartz Cylinders. To employ quartz cylinders for biophysical experiments in an OTW, DNA (or other biomolecules) should be controllably bound to the top surface of quartz cylinder (Figure 1b), and ideally specifically to only the center of the top surface.[13] Our selective functionalization (Figure 2, Steps 10−13, 11a−13a) is demonstrated by its application to both cylinders without protrusions and cylinders with protrusions (Figure 5).

We have tested the selective functionalization of cylinders without protrusions by examining their ability to specifically bind fluorescently labeled biotinylated oligonucleotides (Methods). As shown in

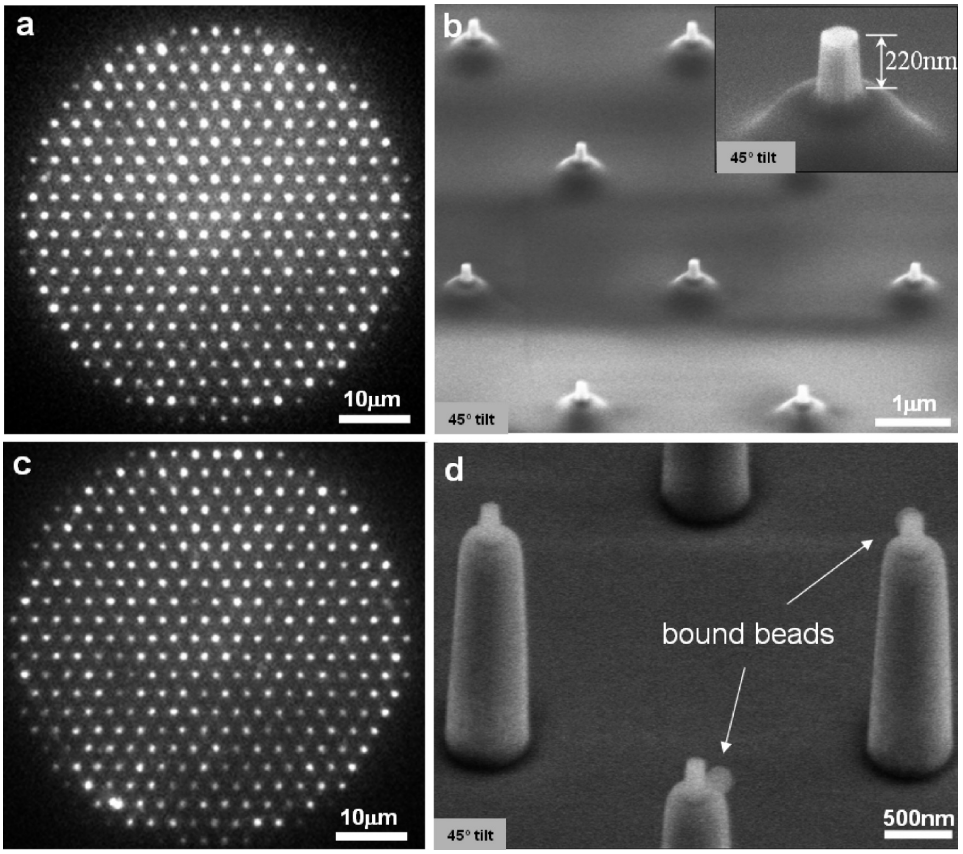

Figure 5. Selective functionalization of micrometer-scale quartz cylinders. (a) Fluorescence image of surface-bound biotinylated, TAMRA-labeled oligonucleotides on a wafer of quartz cylinders without protrusions. The hexagonal pattern of the fluorescent spots (white) indicates that the oligonucleotides specifically bind to the functionalized portion of cylinder surface (primarily the top surface). (b) The centered protrusions of quartz cylinders are exposed for chemical functionalization, while the rest of cylinder surface remains buried and protected in PMMA resist. The inset shows a zoom on a single centered protrusion. (c) Same as in panel a, with the difference that the quartz cylinders have centered protrusions. (d) SEM image of biotinylated microspheres specifically bound to the functionalized centered protrusions of quartz cylinders.

Figure 5a, the fluorescence of bound oligonucleotides appears nearly exclusively at positions that arrange into a hexagonal array, indicating that labeled oligonucleotides do not aspecifically bind to the wafer surface. As both the cylinder's side-wall and the cylinder-free area of the wafer were similarly protected during chemical functionalization, it is likely that the formerly protected portion of the cylinder's sides should lack any specific binding sites. Thus, the chemical functionalization appears limited to the exposed portion of cylinder surface, which is predominantly the top surface.

The selective functionalization of cylinders with centered protrusions was tested similarly. However, to carry out the functionalization a critical step is involved, namely exposing the centered protrusion for chemical functionalization while the rest of the cylinder surface remains buried in PMMA resist (Figure 5b). Given the variability in cylinder height discussed above, one might expect the degree of exposure of the centered protrusion to vary with the radial position on the wafer. While this was indeed the case, the variation in the height of the exposed portion of centered protrusions was interestingly far smaller than the variation in the cylinder height. For example, we find the height of the cylinder main body to increase by ~300 nm (from ~1.7 μm at the wafer center to ~2 μm at 30 mm from wafer center), while the height of the exposed portion of centered protrusion increases by only about 100 nm (from ~120 to ~220 nm). This may be explained by an inhomogeneity in the thickness of the PMMA coating that would partly compensate the variation in cylinder height. We have indeed observed that the PMMA layer displays a slightly undulatory pattern, with maxima on the individual buried cylinders that additionally correlate with their height. With this in mind, we simply designed protrusions of sufficient height (~250−300 nm), thereby ensuring that all centered protrusions were partly exposed and that the remainder of surface was well-protected by PMMA. The selective functionalization of cylinders with centered protrusions was then tested by the specific binding of fluorescently labeled biotinylated oligonucleotides as above (Figure 5c). Again, a hexagonal array of fluorescent spots (of specifically bound oligonucleotides) indicates the chemical functionalization was

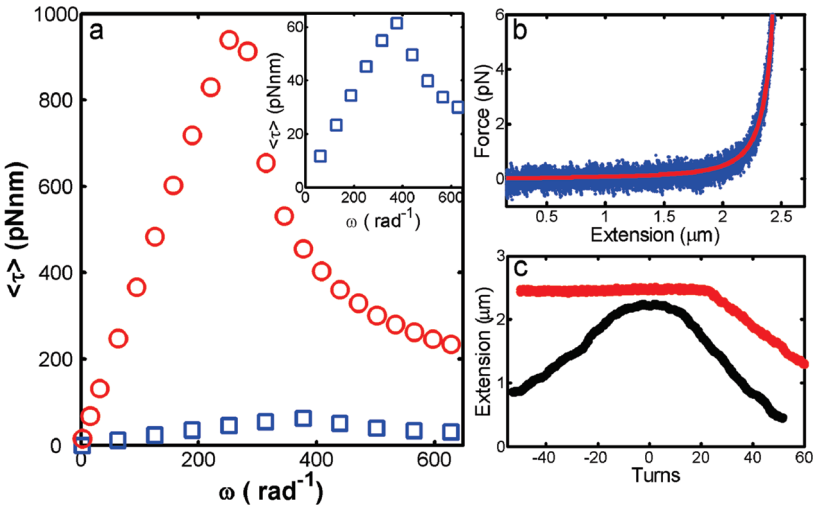

Figure 6. Characterization of quartz cylinders in an OTW. (a) The average torque exerted on an untethered quartz cylinder as a function of rotational frequency. Data are shown in red circles for a large cylinder (cone-shaped with 500 nm top diameter, Figure 3d) and in blue squares for a smaller cylinder (200 nm top diameter, Figure 3c). The inset shows a zoom on the data for the smaller cylinder. At each rotational frequency, the optical torque was recorded for 5 s. (b) Force−extension curve of a dsDNA attached to a quartz cylinder with a centered protrusion (blue points). The red curve shows a fit to the worm-like chain model. (c) Rotation−extension curves of a dsDNA attached to a quartz cylinder with a centered protrusion under stretching forces of 0.5 pN (black points) and 2 pN (red points). The rate of laser polarization rotation equaled 1 turn/s.

specific to the selectively functionalized portion of the centered protrusions. Further evidence for the selectivity of the chemical functionalization was evidenced by direct SEM imaging (Figure 5d), which demonstrated that biotin-labeled microspheres specifically bind to the centered protrusions of quartz cylinders.

Applications of Fabricated Cylinders in the OTW. We now demonstrate the angular trapping properties of quartz cylinders in the OTW (Methods). First, for untethered cylinders of two different diameters (200 nm, 500 nm), we measured torque-rotation curves (Figure 6a; 500 nm cylinder in blue squares, 200 nm cylinder in red circles). Here, the cylinders are rotated at different speeds while measuring the mean value of the exerted torque. We clearly observe two distinct regimes in the response, separated by a threshold frequency: below the threshold frequency, the mean torque increases linearly with the imposed frequency, while subsequently the mean torque decays toward zero.[10,22] The slope in the linear regime is equal to the rotational drag coefficient, which is itself approximately proportional to the cylinder's volume.[31] As expected, therefore, the larger cylinder presents a larger slope: the drag coefficient determined from the slope is about 3.7 pN·nm·s for the large cylinder (~500 nm/900 nm/2 μm, top diameter/bottom diameter/height, Figure 3d), and about 0.18 pN·nm·s for the small cylinder (~200 nm/300 nm/650 nm, Figure 3c). For comparison, theoretical estimation[31] of the rotational drag coefficient in water yields 3.2 pN·nm·s for a large cylinder (700 nm/700 nm/2 μm) and 0.14 pN·nm·s for a small cylinder (250 nm/250 nm/650 nm). While the drag coefficient differs greatly between the small and large cylinders, the same is not true for the threshold frequencies. This is because the maximal possible torque exerted on a cylinder is also roughly proportional to the volume of the cylinder.[23] In other words, given a constant laser power, a larger torque always comes with a larger drag. Note that differently sized cylinders come with distinct advantages: if large torques need to be applied, larger cylinders should be selected; however, when a fast response time is desired, smaller cylinders with their smaller drag are preferred.

We then extended our measurements to cylinders tethered to dsDNA (Figure 6b,c). Here, we employed cylinders with selectively coated centered protrusions (experiments were equally successful on cylinders selectively coated on only a single face, data not shown). First, we varied the force applied to the cylinders by moving the flow cell by piezo-actuators at a constant speed of 1 μm/min relative to the optical trap center along the direction of laser propagation. The displacement of the tethered cylinder relative to the optical trap center was measured to determine the force, and its absolute position with respect to the flow cell surface yielded the molecule's extension (Figure 6b, blue points). The excellent fit to the worm-like chain model[32] (Figure 6b, red line), yielding a persistence length L_p = 42 nm and contour length L_c = 2.6 μm, demonstrated proper attachment of a single molecule. Next, at a fixed force, we rotated the cylinder, yielding an extension-rotation curve (Figure 6c, two different forces shown; see also Methods). The rotational response of the dsDNA, with its characteristic symmetric response under low forces and asymmetric response to rotation under high forces,[33] demonstrates

that the dsDNA is multiply tethered to the centered protrusion. This demonstrates that electron beam-fabricated quartz cylinders are fully capable of manipulating single biomolecules in the OTW, providing a new tool for their subsequent study.

CONCLUSIONS

We have developed a novel method based on electron beam lithography for the fabrication of quartz cylinders. In comparison to approaches based on optical lithography, our method provides far greater versatility: a larger range of cylinder dimensions and more complex geometries were fabricated, under conditions of across-wafer uniformity. We have also developed a novel approach for the selective functionalization of quartz cylinders, which was demonstrated successfully through its use in the stretching and twisting of DNA in an OTW.

METHODS

Fabrication and Functionalization of Quartz Cylinders. Fabrication of the quartz cylinders was performed on 100 mm diameter x-cut single-crystal quartz wafers (University Wafer, USA) and comprised 14 principal steps (Figure 2).

In the first step, the wafers were ultrasonically cleaned in fuming nitric acid (100% HNO_3) for 10 min (Figure 2, Step 1), rinsed in deionized (DI) water and spun dry. Then, the wafer surface was primed for resist adhesion using hexamethyldisilazane by spin-coating at 1000 rpm for 55 s (Figure 2, Step 2). For the fabrication of small cylinders (height <0.8 μm, Figure 3a−c), after priming, a 380 nm layer of NEB-22A2E negative electron-beam resist (Sumitomo Chemical Co.) was spin-coated onto the wafer at 1000 rpm for 55 s and baked for 3 min at 110 °C (Figure 2, Step 3). For the fabrication of larger cylinders (height > 1.5 μm, Figure 3d−f), it was necessary to apply a thicker layer of resist. In this case, the solution of NEB-22A2E resist was first spread out on the wafer by spin-coating at 500 rpm for 4 s, after which the resist solution was concentrated by evaporating the solvent on the wafer for 3 min in the spin-coater. The wafer was subsequently spun at 1000 rpm for 55 s and baked for 3 min at 110 °C. The layer of NEB-22A2E resist prepared by this method has a uniform-film thickness of about 1.4−1.6 μm, which greatly exceeds the maximum possible spin-coated thickness as determined by the resist solvent content and specified by the resist supplier. Following the spin-coating of resist, a 20 nm gold layer is deposited on top of the resist (Figure 2, Step 4) using a resistive thermal evaporator (Leybold-Heraeus L560). This gold layer serves as a reflective layer to facilitate the focusing on the electron beam lithography machine (Leica EBPG 5000+) and additionally provides a charge dissipation path during electron beam exposure. At this point, the sample is ready for patterning.

Feature patterning (Figure 2, Step 5) is performed on a Leica EBPG 5000+ (acceleration voltage 100 kV, aperture 400 μm). The cylinders were exposed as single pixels, whereby the pixel size was adjusted by defocusing a small electron spot to reduce the irregularity of the feature shape. Nominal pixel diameters of 200 nm (Figure 3c), 300 nm (Figure 3a,b), and 500 nm (Figure 3d−f) were achieved by defocusing electron spots with currents of 9, 12, and 38 nA (corresponding to estimated 12, 14, and 24 nm before defocusing, respectively). Doses equaled 5000 μC/cm^2 with a 20 nm beam step size (BSS) (for 200 and 300 nm pixels) or 100 μC/cm^2 with a 200 nm BSS (for 500 nm pixels). The beam settling time was set to 10 μs to minimize the overall patterning time (per billion cylinders, machine time was ~10 h for 200 and 300 nm pixel sizes, and ~8.5 h for 500 nm pixel sizes). Cylinders were arranged in a hexagonal array with pitches of 1 μm (for 200 or 300 nm cylinders) or 3 μm (for 500 nm cylinders), yielding a total of 0.4−0.8 billion cylinders.

Following electron beam exposure, the resist was baked at 105 °C for 3 min and the gold overcoat was removed by immersing the wafer in gold etchant TFA (Transene, USA) for ~20 s (Figure 2, Step 6), rinsing with DI water, and spinning dry. Next, the development was done for 1 min in Microposit MF322 solution (Rohm and Haas), followed by a 15 s soaking in 1:10 diluted MF322 solution (Figure 2, Step 7). The wafer was then rinsed in DI water and spun dry. The wafers were then dry-etched (Figure 2, Step 8) in an inductive-coupled-plasma (ICP) reactive-ion etcher (Adixen AMS100 I-speeder) with a mixture of 20 sccm C_4F_8 and 10 sccm CH_4, diluted in 100 sccm He. The ICP source power equaled 2500 W, and the substrate bias RF power equaled 300 W, except for the etching of cone-shaped cylinders (Figure 3d), where the RF bias power equaled 250 W. The pressure was maintained as low as possible, ~1 Pa. The temperature was maintained at 0 °C for the sample holder and 200 °C for the chamber. Under these settings, for both the 300 and 250 W RF bias power, the etching rate of quartz was ~170 nm/min at the wafer center and ~200 nm/min at a radial distance of 30 mm from the wafer center, and the etch selectivity of the quartz relative to the resist masks was ~3:1.

For the fabrication of cylinders with centered protrusions (Figure 3f), two additional steps followed dry etching. First, the wafer was exposed to O_2 plasma in a microwave plasma system (Tepla 100, TePla AG, Germany) to shrink the size of the resist residues (Figure 2, Step 8a).[13] The microwave power equaled 100 W, and the pressure was kept at 0.15 mbar with a 30-sccm O_2 flow. This resulted in isotropic etching of the resist at a nearly uniform rate of ~10 nm/min across the wafer. Second, the wafer was reloaded into the reactive-ion etcher to undergo an additional C_4F_8 plasma etching for 90 s using the same settings as above (Figure 2, Step 8). This resulted in the formation of small protrusions (Figure 2, Step 8b).

Following the C_4F_8 plasma etching, the wafer was cleaned by O_2 plasma (Figure 2, Step 9), in the Adixen etcher to remove residues of the resist mask and Teflon-like polymers deposited during the dry etching process.

We next proceeded with selective surface functionalization (Figure 2, Steps 10−13). First, to bury the cylinders, the wafers were spin-coated with a layer of PMMA 950 k resist (Figure 2, Step 10) that was determined to initially exceed the height of the quartz cylinders by ~100 nm. Its thickness was then reduced by exposure to O_2 plasma (settings as in Step 8a of Figure 2). For cylinders without protrusions (Figure 3b−d), the final PMMA thickness was *ca.* 10−30 nm thinner than the cylinder height, just exposing the cylinders' top surface for functionalization (Figure 2, Step 11). For cylinders with protrusions, the resist thickness was reduced to a lesser extent so that only the protrusions were accessible for surface functionalization (Figure 2, Step 11a; Figure 5b). In both cases, the exposed surfaces were amino-functionalized by immersing in 1% Vectabond (Vector Laboratories, Burlingame, CA) in isopropyl alcohol for 5 min, followed by rinsing with DI water and drying by spinning (Figure 2, Steps 12, 12a). A further step yielded the desired functional group on the surface; for example, to obtain biotinylated cylinders the wafer of amino-functionalized cylinders was immersed in 2 mg/mL EZ-Link Sulfo-NHS-LC-LC-Biotin (Pierce Chemical Co.) dissolved in Na_2CO_3 buffer (100 mM, pH 8.5) for 2 h, followed by rinsing with DI water and spinning dry. Finally, the PMMA resist was removed with acetone in an ultrasonic bath for 5 min (Figure 2, Steps 13, 13a), and the wafer was rinsed with DI water and spun dry.

In the final step of the protocol, the quartz cylinders were shaved off from the wafer (Figure 2, Step 14) using a clean

microtome blade (DT315D50, C. L. Sturkey, Inc.)[21] and stored in TE buffer (10 mM Tris-HCl, 1 mM EDTA, pH 7.5).

Size Measurement of Quartz Cylinders. Characterization of the quartz cylinders (Figure 3) was conducted *via* scanning electron microscopy (SEM) using a Hitachi S4800 and a FEI/Philips XL30S/FEG. A wafer of 300 nm cylinders (Figure 2a,b) was used to characterize the uniformity of cylinder dimensions across a wafer (Figure 4). In this measurement, 20 SEM images of individual cylinders were obtained from different radial positions on the wafer. Dimensions of the cylinders were directly deduced from the SEM images with an accuracy of ~8 nm per pixel.

Testing the Functionalization of Quartz Cylinders. The functionalization of the quartz cylinders' top surfaces was tested (Figure 5a) by the binding specificity of fluorescently labeled biotinylated oligonucleotides (biotin-5′-ttagggttagggttaggg-TAMRA, Biolegio). Using the same approach, we also tested the functionalization of the cylinders with centered protrusions (Figure 5c); the latter result was confirmed by direct SEM imaging of the binding of 200 nm biotinylated microspheres (FluoSpheres F8767, Invitrogen) onto the functionalized cylinder protrusions (Figure 5d).

To bind labeled oligonucleotides, the wafer of selectively biotinylated cylinders (with or without protrusions) was first treated with 10 μg/mL streptavidin (Sigma) in PBS buffer (137 mM NaCl, 2.7 mM KCl, 10 mM Na_2HPO_4, 1.76 mM KH_2PO_4, pH 7.4) for 20 min, rinsed with DI water, and spun dry. Next, 1 mg/mL bovine serum albumin (BSA; Sigma) in PBS buffer was applied onto the wafer for 20 min to prevent nonspecific binding, followed by DI water rinsing and spinning dry. Then, labeled oligonucleotides (10 nM, in PBS buffer) were incubated with the cylinders for 20 min, followed by rinsing with DI water and spinning dry. Subsequently, the wafer of cylinders was imaged using a wide-field fluorescence microscope (IX71, Olympus, Japan) equipped with a 532 nm diode-pumped laser (GCL-050-L-0.5%, Crystalaser, USA). To do so, the wafer was mounted up-side-down on the microscope. Movies (0.1 s exposure time) were recorded, for which the first frames are shown in Figure 5a (cylinders without protrusions) and Figure 5c (cylinders with protrusions).

To test the binding specificity with biotin-labeled microspheres, we employed the same wafer as above. Therefore, the wafer was first ultrasonically cleaned to remove any remaining organic coating in fuming nitric acid for 10 min, rinsed in DI water and spun dry. Next, the cylinders were selectively refunctionalized with Vectabond and EZ-Link Sulfo-NHS-LC-LC-Biotin as above (Figure 2, Steps 11a−13a). The wafer was then treated with steptavidin and BSA. A solution of 200 nm biotinylated microspheres was incubated with the wafer for 20 min, followed by rinsing with DI water and spinning dry. The specific binding of biotinylated microspheres was then visualized by SEM (Figure 5d).

OTW Instrumentation. To constitute the OTW,[10] the laser (Coherent Compass CW Nd:VO_4 1064−4000M) was linearly polarized and focused by a 60× objective (CFI-PLAN-APO-VC-60XA-WI, Nikon) into a custom-made glass flow cell mounted onto piezo-actuators (P-517.3CD, Physik Instrumente). We used a fast electro-optical modulator (EOM; LM 0202-LT, LINOS) in combination with a quarter-wave plate (PWPS-1064-10-4, CVI Melles Griot) as a polarization control system. The torque transferred to the trapped particle was measured optically (Figure 1c) by two identical fast intensity detectors (DET10C/M, Thorlabs) from the imbalance of the two circular components of the polarization at the trap output, separated using a quarter-wavelength plate and a polarizing beam splitter (PBS-1064-100, CVI Melles Griot). The linear displacement of the quartz cylinder in the trap (and hence the force), as well as its height above the surface, were detected *via* a position-sensitive device (PSD; DL100-7PCBA3, Pacific Silicon Sensor). To obtain constant force, the force measurement was fed back to the piezo-actuators to adjust the linear displacement of the trapped particle, clamping the force at a specified set point. For measurements of quartz cylinders in the OTW, the power entering the objective equaled 100 mW and data was acquired at 100 kHz.

Flow Cell Assembly and DNA Constructs. Flow cells were assembled from microscope coverslips with a parafilm spacer. For experiments on quartz cylinders alone, the bottom surface was coated with nitrocellulose (0.01% (wt/vol) in amyl acetate), followed by an incubation of 10 mg/mL BSA for 30 min to prevent nonspecific adhesion of quartz cylinders (prepassivated with 5 mg/mL BSA for 20 min prior to introduction into the flow cell). For experiments on quartz cylinders bound to DNA, an incubation of the flow cell with 0.1 mg/mL antidigoxigenin (Roche) in PBS for 30 min (to provide for DNA attachment) preceded the BSA incubation.

We used 7.9 kb dsDNA molecules ligated at their two extremities to ~0.6 kb PCR fragments functionalized with multiple biotin and digoxigenin groups, respectively.[25] dsDNA constructs were incubated in the passivated flow cell for 30 min in tethering buffer (320 mM NaCl, 10 mM Tris-HCl, 1 mM EDTA, pH 7.5) and then again for 30 min in the presence of an additional 0.1 mg/mL streptavidin. Then the quartz cylinders (with biotinylated protrusions), which had been prepassivated in 5 mg/mL BSA for 20 min, were added, to be followed by an additional 30 min incubation. Following each incubation step, the flow cell was flushed thoroughly with tethering buffer. After the final flushing step, only the dsDNA-tethered cylinders remained in the flow cell.

Acknowledgment. We thank M. Zuiddam for help with the C_4F_8 dry etching protocol, A. van Run for assistance in optimizing the electron beam exposure, M. van der Krogt for help with gold deposition, P. Galajda, E. van der Drift, and J. Andreasson (Stanford University) for advice on microfabrication, S. Hage and S. Donkers for DNA synthesis, J. van der Does, D. de Roos, and J. Beekman for help with instrumentation and infrastructure, F. Hol for stimulating discussions, TU Delft Nanofacility for process support, and TU Delft, FOM (Dutch Foundation for Research on Matter), NWO (Nederlandse Organisatie voor Wetenschappelijk Onderzoek), and ESF (European Science Foundation) for financial support.

REFERENCES AND NOTES

1. Pankhurst, Q. A.; Connolly, J.; Jones, S. K.; Dobson, J. Applications of Magnetic Nanoparticles in Biomedicine. *J. Phys. D* **2003,** *36*, R167–R181.
2. Neuman, K. C.; Nagy, A. Single-Molecule Force Spectroscopy: Optical Tweezers, Magnetic Tweezers and Atomic Force Microscopy. *Nat. Methods* **2008,** *5*, 491–505.
3. Walter, N. G.; Huang, C. Y.; Manzo, A. J.; Sobhy, M. A. Do-It-Yourself Guide: How to Use the Modern Single-Molecule Toolkit. *Nat. Methods* **2008,** *5*, 475–489.
4. Svoboda, K.; Block, S. M. Biological Applications of Optical Forces. *Annu. Rev. Biophys. Biomol. Struct.* **1994,** *23*, 247–285.
5. Kegel, W. K.; van Blaaderen, A. Direct Observation of Dynamical Heterogeneities in Colloidal Hard-Sphere Suspensions. *Science* **2000,** *287*, 290–293.
6. Pertsinidis, A.; Ling, X. S. Diffusion of Point Defects in Two-Dimensional Colloidal Crystals. *Nature* **2001,** *413*, 147–150.
7. Ghosh, A.; Fischer, P. Controlled Propulsion of Artificial Magnetic Nanostructured Propellers. *Nano Lett.* **2009,** *9*, 2243–2245.
8. Bishop, A. I.; Nieminen, T. A.; Heckenberg, N. R.; Rubinsztein-Dunlop, H. Optical Microrheology Using Rotating Laser-Trapped Particles. *Phys. Rev. Lett.* **2004,** *92*, 198104.
9. Parkin, S. J.; Knoner, G.; Nieminen, T. A.; Heckenberg, N. R.; Rubinsztein-Dunlop, H. Picoliter Viscometry Using Optically Rotated Particles. *Phys. Rev. E* **2007,** *76*, 041507.
10. Pedaci, F.; Huang, Z.; van Oene, M.; Barland, S.; Dekker, N. H., Excitable Particles in an Optical Torque Wrench. *Nat. Phys.* in press.
11. Leach, J.; Mushfique, H.; di Leonardo, R.; Padgett, M.; Cooper, J. An Optically Driven Pump for Microfluidics. *Lab Chip* **2006,** *6*, 735–739.
12. Forth, S.; Deufel, C.; Sheinin, M. Y.; Daniels, B.; Sethna, J. P.; Wang, M. D. Abrupt Buckling Transition Observed During the Plectoneme Formation of Individual DNA Molecules. *Phys. Rev. Lett.* **2008,** *100*, 148301.

13. Gutierrez-Medina, B.; Andreasson, J. O. L.; Greenleaf, W. J.; LaPorta, A.; Block, S. M. An Optical Apparatus for Rotation and Trapping. *Method Enzymol.* **2010,** *474*, 377–404.
14. Vogel, R.; Persson, M.; Feng, C.; Parkin, S. J.; Nieminen, T. A.; Wood, B.; Heckenberg, N. R.; Rubinsztein-Dunlop, H. Synthesis and Surface Modification of Birefringent Vaterite Microspheres. *Langmuir* **2009,** *25*, 11672–11679.
15. Parkin, S. J.; Vogel, R.; Persson, M.; Funk, M.; Loke, V. L. Y.; Nieminen, T. A.; Heckenberg, N. R.; Rubinsztein-Dunlop, H. Highly Birefringent Vaterite Microspheres: Production, Characterization and Applications for Optical Micromanipulation. *Opt. Express* **2009,** *17*, 21944–21955.
16. Singer, W.; Nieminen, T. A.; Gibson, U. J.; Heckenberg, N. R.; Rubinsztein-Dunlop, H. Orientation of Optically Trapped Nonspherical Birefringent Particles. *Phys. Rev. E* **2006,** *73*, 021911.
17. Singer, W.; Rubinsztein-Dunlop, H.; Gibson, U. Manipulation and Growth of Birefringent Protein Crystals in Optical Tweezers. *Opt. Express* **2004,** *12*, 6440–6445.
18. Starr, C.; Dultz, W.; Wagner, H. P.; Dholakia, K.; Schmitzer, H. Optically Controlled Rotation of PTCDA Crystals in Optical Tweezers. *AIP Conf. Proc.* **2005,** *772*, 1099–1100.
19. Sun, X. D.; Zhang, H. L.; Li, X. C.; Gong, D. W.; Lee, H. Optical Rotation and Manipulation of Micro-Sized $LiNbO_3$ Crystals and Single-Walled Carbon Nanotubes Bundles. *Colloid Surf., A* **2008,** *313*, 488–491.
20. Rodriguez-Otazo, M.; Augier-Calderin, A.; Galaup, J. P.; Lamere, J. F.; Fery-Forgues, S. High Rotation Speed of Single Molecular Microcrystals in an Optical Trap with Elliptically Polarized Light. *Appl. Opt.* **2009,** *48*, 2720–2730.
21. Deufel, C.; Forth, S.; Simmons, C. R.; Dejgosha, S.; Wang, M. D. Nanofabricated Quartz Cylinders for Angular Trapping: DNA Supercoiling Torque Detection. *Nat. Methods* **2007,** *4*, 223–225.
22. La Porta, A.; Wang, M. D. Optical Torque Wrench: Angular Trapping, Rotation, and Torque Detection of Quartz Microparticles. *Phys. Rev. Lett.* **2004,** *92*, 190801.
23. Friese, M. E. J.; Nieminen, T. A.; Heckenberg, N. R.; Rubinsztein-Dunlop, H. Optical Alignment and Spinning of Laser-Trapped Microscopic Particles. *Nature* **1998,** *394*, 348–350.
24. Ashkin, A.; Dziedzic, J. M.; Yamane, T. Optical Trapping and Manipulation of Single Cells Using Infrared-Laser Beams. *Nature* **1987,** *330*, 769–771.
25. Lipfert, J.; Kerssemakers, J. W.; Jager, T.; Dekker, N. H., Magnetic Torque Tweezers: Measuring Torsional Stiffness in DNA and Reca-DNA Filaments. *Nat. Methods* 2010.
26. Westerheim, A. C.; Labun, A. H.; Dubash, J. H.; Arnold, J. C.; Sawin, H. H.; Yuwang, V. Substrate Bias Effects in High-Aspect-Ratio Sio2 Contact Etching Using an Inductively-Coupled Plasma Reactor. *J. Vac. Sci. Technol., A* **1995,** *13*, 853–858.
27. Karttunen, J.; Kiihamaki, J.; Franssila, S. Loading Effects in Deep Silicon Etching. *SPIE* **2000,** *4174*, 90–97.
28. Akashi, T.; Yoshimura, Y. Deep Reactive Ion Etching of Borosilicate Glass Using an Anodically Bonded Silicon Wafer as an Etching Mask. *J. Micromech. Microeng.* **2006,** *16*, 1051–1056.
29. Kiihamaki, J. Deceleration of Silicon Etch Rate at High Aspect Ratios. *J. Vac. Sci. Technol., A* **2000,** *18*, 1385–1389.
30. Kokkoris, G.; Gogolides, E.; Boudouvis, A. G. Simulation of Fluorocarbon Plasma Etching SiO_2 Structures. *Microelectron. Eng.* **2001,** *57−8*, 599–605.
31. Tirado, M. M.; Garciadelatorre, J. Rotational-Dynamics of Rigid, Symmetric Top Macromolecules— Application to Circular-Cylinders. *J. Chem. Phys.* **1980,** *73*, 1986–1993.
32. Bustamante, C.; Marko, J. F.; Siggia, E. D.; Smith, S. Entropic Elasticity of Lambda-Phage DNA. *Science* **1994,** *265*, 1599–1600.
33. Strick, T. R.; Dessinges, M. N.; Charvin, G.; Dekker, N. H.; Allemand, J. F.; Bensimon, D.; Croquette, V. Stretching of Macromolecules and Proteins. *Rep. Prog. Phys.* **2003,** *66*, 1–45.